nature physics

SUPPLEMENTARY INFORMATION
https://doi.org/10.1038/s41567-018-0400-9

In the format provided by the authors and unedited.

Synthesis of antisymmetric spin exchange interaction and chiral spin clusters in superconducting circuits

Da-Wei Wang[1,2,3*], Chao Song[1], Wei Feng[1,4], Han Cai[1], Da Xu[1], Hui Deng[5], Hekang Li[5,6], Dongning Zheng[3,5,6], Xiaobo Zhu[7*], H. Wang[1*], Shi-Yao Zhu[1,7] and Marlan O. Scully[2]

[1]Interdisciplinary Center for Quantum Information, Department of Physics and State Key Laboratory of Modern Optical Instrumentation, Zhejiang University, Hangzhou, Zhejiang, China. [2]Institute of Quantum Science and Engineering, Texas A&M University, College Station, TX, USA. [3]CAS Center of Excellence in Topological Quantum Computation, Beijing, China. [4]Beijing Computational Science Research Center, Beijing, China. [5]Institute of Physics, Chinese Academy of Sciences, Beijing, China. [6]School of Physical Sciences, University of Chinese Academy of Sciences, Beijing, China. [7]Synergetic Innovation Center of Quantum Information and Quantum Physics, University of Science and Technology of China, Hefei, Anhui, China.
*e-mail: dwwang@zju.edu.cn; xbzhu16@ustc.edu.cn; hhwang@zju.edu.cn

Supplementary Information for: Synthesis of antisymmetric spin exchange interaction and chiral spin clusters in superconducting circuits

DEVICE

Our device consists of five frequency-tunable superconducting transmon qubits, named from Q_a to Q_e, interconnected by a bus resonator which has a fixed-frequency ω_r. The qubit transition frequency is set at ω_j for state initialization and measurement, where single-qubit rotation gates are applied. g_j is the on-resonance coupling strength between each qubit and the bus resonator. The qubit anharmonicity η_i equals to the transition-frequency difference between the ground to first-excited states and the first-excited to second-excited states. All relevant device parameters are experimentally measured and are listed in Tab. S1.

ASI HAMILTONIAN

In the following we show the derivation of Eq. (3) in the main text. The quantity

$$\begin{aligned}4\sqrt{3}S_zC_z &= \sum_j \sigma_j^z \sum_{j'} \sigma_{j'}^z \left(\sigma_{j'+1}^x\sigma_{j'+2}^y - \sigma_{j'+1}^y\sigma_{j'+2}^x\right), \\ &= \sum_j \left(\sigma_{j+1}^x\sigma_{j+2}^y - \sigma_{j+1}^y\sigma_{j+2}^x\right) \\ &+ \sum_j \left(\sigma_j^z + \sigma_{j+1}^z\right)\left(\sigma_j^x\sigma_{j+1}^y - \sigma_j^y\sigma_{j+1}^x\right), \quad \text{(S1)}\end{aligned}$$

where we have used $\sigma_j^z\sigma_j^z = 1$ and the summation indices j and j' run cyclically from 1 to 3. The second summation $\left(\sigma_j^z + \sigma_{j+1}^z\right)\left(\sigma_j^x\sigma_{j+1}^y - \sigma_j^y\sigma_{j+1}^x\right) = 0$, since $\sigma_j^z\sigma_j^x = i\sigma_j^y$. The first term is $4\sqrt{3}\sum_{j=1}^3 \mathbf{D}\cdot(\boldsymbol{\sigma}_j \times \boldsymbol{\sigma}_{j+1})$, which proves Eq. (3) in the main text.

GAUGE-INVARIANCE

Here we only study the antisymmetric spin exchange interaction, which means that a phase of $\pi/2$ or a phase factor of $e^{i\pi/2}$ is gained in each transition. For any closed loop in Figs. 2 and 3 in the main text, the accumulated phase (magnetic flux) is either $\pi/2$ or $-\pi/2$. We need to verify the gauge-invariance of the total phase, since the antisymmetric interaction is induced by modulation techniques, which is unconventional. We take a loop that contains three spins numbered by 1, 2 and 3 for example. The phase accumulation in each of the transitions depends on the phases of the qubit-resonator coupling strengths g_1, g_2 and g_3, which are assumed real in our experiments. However, we can make a gauge transformation of the spin-up state of the jth qubit $|\uparrow_j\rangle \rightarrow e^{i\phi_j}|\uparrow_j\rangle$. In the new basis, the coupling strength is transformed according to $g_j \rightarrow e^{-i\phi_j}g_j$. The effective ASI strength between the spins i and j is transformed as $\kappa_{i,j} = e^{i(\phi_i - \phi_j)}\kappa$, which is gauge-dependent. However, in the loop, the total phase is transformed by summing over all the phases due to the gauge transformation, i.e., $\Phi \rightarrow \Phi + \phi_1 - \phi_2 + \phi_2 - \phi_3 + \phi_3 - \phi_1 = \Phi$, which is gauge-invariant. The dynamics is determined by the total phase Φ. In various ASI configurations in Figs. 2 and 3 in the main text, there are many loops and some loops involve more than 3 spins. The gauge-invariance is still valid in these cases. If the loop that contains N spins and each spin has a gauge transformation $|\uparrow_j\rangle \rightarrow e^{i\phi_j}|\uparrow_j\rangle$, the total phase in the loop is transformed according to $\Phi \rightarrow \Phi + \phi_1 - \phi_2 + \phi_2 - \phi_3 + ... + \phi_N - \phi_1 = \Phi$, which is invariant.

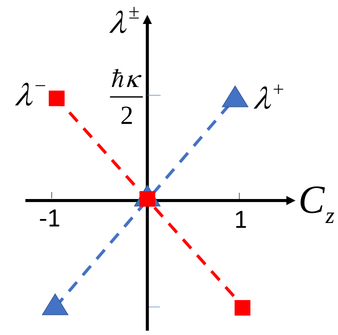

Figure S1. **Energy spectra of the Hamiltonian in Eq. (3) in the main text.** Blue triangles and red squares are for $\lambda^+(C_z)$ and $\lambda^-(C_z)$, respectively.

EIGENSTATES AND DISPERSION RELATION

The chiral dynamics in Fig. 2 in the main text can be explicitly calculated from the dispersion relation of the Hamiltonian, as shown in Fig. S1. Since $[C_z, S_z] = 0$, the eigenspace of H can be constructed by the eigenstates of C_z and S_z, denoted by their eigenvalues $|C_z, S_z\rangle$. In the subspace of $S_z = \pm 1/2$, the eigenenergies are $\lambda^{\pm}(C_z) = \pm C_z\hbar\kappa/2$ with $C_z = 0, \pm 1$ and the corresponding spin-wave eigenstates are

$$|C_z, -1/2\rangle = \frac{1}{\sqrt{3}}\left(|\uparrow\downarrow\downarrow\rangle + e^{2iC_z\pi/3}|\downarrow\uparrow\downarrow\rangle + e^{4iC_z\pi/3}|\downarrow\downarrow\uparrow\rangle\right), \quad \text{(S2)}$$

Table S1. **Device parameters**. Listed are the experimentally measured bus resonator's resonant frequency and energy relaxation time, as well as each qubit's idle frequency ω_j, anharmonicity η_j, coupling strength to the bus resonator g_j, energy relaxation time $T_{1,j}$, and Gaussian dephasing time $T^*_{2,j}$. The column R is for the parameters of the bus resonator. Two devices of the same design are used in our experiment, and the parameters listed in parentheses are for the second device.

	Q_a	Q_b	Q_c	Q_d	Q_e	R
$\omega_j/2\pi$ (GHz)	5.204 (5.400)	5.897 (5.300)	5.287 (5.060)	5.253 (5.350)	5.341 (6.020)	5.585 (5.643)
$\eta_j/2\pi$ (MHz)	245 (243)	242 (243)	245 (243)	243 (243)	244 (243)	/
$g_j/2\pi$ (MHz)	20.9 (20.0)	20.6 (19.7)	20.1 (20.9)	18.8 (19.9)	19.8 (19.6)	/
$T_{1,j}$ (μs)	20.2 (13.3)	10.2 (13.9)	18.9 (19.9)	19.2 (13.1)	13.9 (9.1)	13.0 (9.8)
$T^*_{2,j}$ (μs)	1.1 (1.5)	4.3 (1.3)	1.3 (3.4)	0.7 (1.2)	1.7 (2.6)	/

and

$$|C_z, +1/2\rangle = \frac{1}{\sqrt{3}}(|\downarrow\uparrow\uparrow\rangle + e^{2iC_z\pi/3}|\uparrow\downarrow\uparrow\rangle + e^{4iC_z\pi/3}|\uparrow\uparrow\downarrow\rangle). \tag{S3}$$

By uniformly placing the three spins on a unit circle and labelling their positions by $0, 2\pi/3, 4\pi/3$, we can understand $C_z = 0, \pm 1$ as the momenta of the spin waves. For dynamics of spin configurations $|\uparrow\downarrow\downarrow\rangle$ and $|\downarrow\uparrow\uparrow\rangle$, which are spin wave packets, their group velocities are,

$$v_g^{\pm} = \frac{\partial \lambda^{\pm}(C_z)}{\hbar \partial C_z} = \pm\kappa/2. \tag{S4}$$

It costs a time $T_0 = 2\pi/3|v_g^{\pm}| = 4\pi/3\kappa$ for the two spin configurations to move for one step (spin site) in opposite directions, which is consistent with Eq. (4) in the main text.

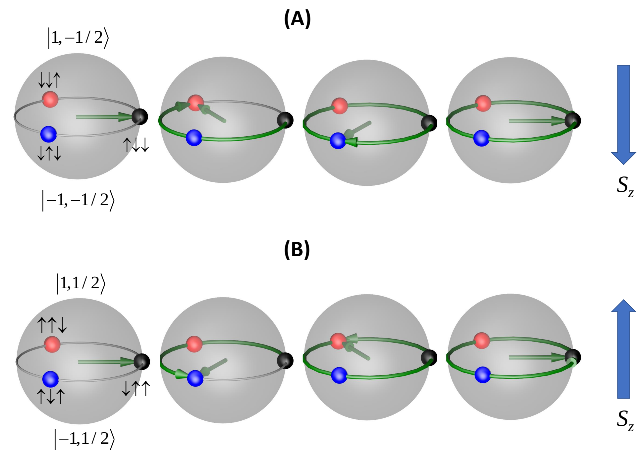

Figure S2. **The chiral spin evolution explained by the precession of the chirality vector.** In the chirality Bloch sphere of the doublet-state subspace with (A) $S_z = +1/2$ and (B) $S_z = -1/2$, we show how the chirality vector $\mathbf{C}$ (indicated by green arrows) precesses around an effective field which is aligned with the corresponding blue arrow on the far right. At multiples of T_0, $\mathbf{C}$ reaches the states with just one spin flipped, as labelled by small color balls on the equator, which are superpositions of a doublet states and a stationary singlet state.

CHIRALITY VECTOR

The dynamics in Fig. 1 in the main text can also be interpreted as a precession of the chirality vector,

$$\mathbf{C} = C_x\hat{x} + C_y\hat{y} + C_z\hat{z}, \tag{S5}$$

where

$$C_x = \frac{1}{12}\left(2\boldsymbol{\sigma}_2\cdot\boldsymbol{\sigma}_3 - \boldsymbol{\sigma}_1\cdot\boldsymbol{\sigma}_2 - \boldsymbol{\sigma}_3\cdot\boldsymbol{\sigma}_1\right), \tag{S6}$$

and

$$C_y = \frac{1}{4\sqrt{3}}\left(\boldsymbol{\sigma}_1\cdot\boldsymbol{\sigma}_2 - \boldsymbol{\sigma}_3\cdot\boldsymbol{\sigma}_1\right). \tag{S7}$$

The three components have the same commutation relation as the Pauli matrices, $[C_i, C_j] = 2\varepsilon_{ijk}C_k$. Therefore, the Hamiltonian $H \propto S_z C_z$ can be understood as that C is subjected to a field along $\hat{z}$ axis with directions depending on S_z, as shown in Fig. S2. The six states $|C_z, S_z\rangle$ can be grouped into two singlets and two doublets of the eigenstates of $\mathbf{C}$. We initially prepare the spins in $|\uparrow\downarrow\downarrow\rangle \equiv |0\rangle/\sqrt{3} + \sqrt{2}|\Uparrow_x\rangle/\sqrt{3}$, where $|0\rangle \equiv |0, -1/2\rangle$ is a singlet eigenstate and does not evolve with time, while $|\Uparrow_x\rangle = (|1,-1/2\rangle + |-1,-1/2\rangle)/\sqrt{2}$ is a doublet eigenstate of C_x with the eigenvalue $C_x = 1$ and precesses on the equator of the chirality Bloch sphere around $S_z\hat{z}$ with $S_z = -1/2$ (and thus the precession is in the opposite direction in the $S_z = 1/2$ subspace), as shown in Fig. S2. After every rotation of $\theta = 4\pi/3$, the wavefunction evolves to a separable state $|\downarrow\downarrow\uparrow\rangle$ and then $|\downarrow\uparrow\downarrow\rangle$ in a chiral way.

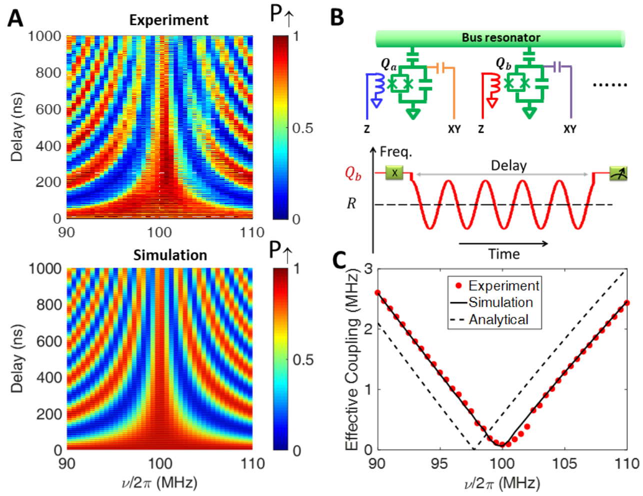

Figure S3. **Tunable effective couplings between the qubit and the resonator.** (A) Experimental data (top) and numerical simulation (bottom) of the vacuum Rabi oscillations between the qubit, Q_b, and the resonator at different modulation frequencies ν, while the modulation amplitude is fixed at $\Delta/2\pi = 235$ MHz. Shown are the qubit $|\uparrow\rangle$ state probabilities $P_\uparrow$ (see color bar on the right) as functions of the delay time along $\hat{y}$ axis. The experimental setup and the pulse sequence are shown in (B), where through its Z bias line the resonant frequency of Q_b is sinusoidally modulated, which centers at the resonant frequency of the resonator ω_r and oscillates with the amplitude Δ and the frequency ν. X is a π rotation around $\hat{x}$ axis driven through Q_b's XY line. (C) Effective coupling strength $|g_0|$ between the qubit and the resonator (red dots) as a function of ν obtained by Fourier transform of the experimental data in A. Also shown are the analytic result with second order approximation (dashed line) and the numerical simulation result that includes high order terms in the Hamiltonian (solid line). The decoupling point for $J_0(f) = 0$ is at $\nu/2\pi$=100 MHz.

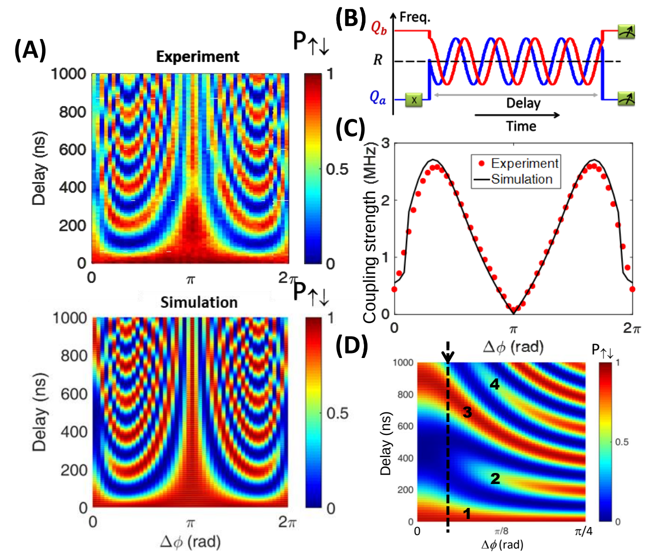

Figure S4. **Tunable effective coupling between two qubits.** (A) Experimental data (top) and simulation (bottom) of two-qubit swap dynamics as a function of the modulation phase difference between the two qubits $\Delta\phi$. The probabilities that Q_a is in the $|\uparrow\rangle$ state and Q_b is in the $|\downarrow\rangle$ state, $P_{\uparrow\downarrow}$, are shown (see color bar on the right) as functions of delay time along y axis. The pulse sequence is shown in (B), where the resonant frequencies of Q_a and Q_b are sinusoidally modulated, both of which center at the resonant frequency of the resonator ω_r and oscillate with the same amplitude Δ and the same frequency ν. Here $\Delta/2\pi = 235$ MHz and $\nu = 100$ MHz for both qubits. The two modulation sinusoids differ by a phase $\Delta\phi$. The experimental setup is shown in Fig. S3 (B). (C) Effective coupling strength $|g_{\rm eff}|$ as a function of $\Delta\phi$ (red dots) obtained by Fourier transform of the experimental data in (A), in comparison with the numerical simulation result (line). (D) Zoom-in view of the numerical simulation result in (A) for $0 \leq \Delta\phi \leq \pi/4$. The colour map identifies a gradual termination of the even-number bright (red) stripes as $\Delta\phi$ approaches below $\pi/16$ (marked by black dash line). As such the effective coupling strength, which is estimated by Fourier transform of the sliced data for fixed $\Delta\phi$, would show a discontinuity (see the sharp drop of the line at small values of $\Delta\phi$ in (C)) where the bright stripes completely disappear. We further confirm that such a discontinuity is associated with a quick rise of the photon number in the central bus resonator, which will be investigated elsewhere.

TUNABLE EFFECTIVE COUPLINGS

The periodic modulation of the transition frequencies of the qubits results in effective couplings between the qubits and the bus resonator and between the qubits. In Fig. S3, we show the tunable control of the qubit-resonator coupling. The effective Hamiltonian between the qubit and the resonator is $H_0 = \hbar g_0 (a\sigma^+ + H.c.)$ with $g_0 = gJ_0(f)$ being the effective coupling strength in the second order perturbation. We excite the qubit and measure its excited-state probability as a function of the delay time at different modulation frequencies, while the modulation amplitude is fixed at $\Delta = 235$ MHz. When $\nu/2\pi \approx 100$ MHz, the effective coupling strength g_0 becomes zero and the qubit is dynamically decoupled from the resonator. From Fig. S3 (C), we can see that the experimental result on the decoupling frequency has a deviation of about 2 MHz from the analytic result estimated using the zero point of $J_0(f)$, which is due to the high order terms in the effective Hamiltonian.

When we have two qubits, Q_a and Q_b, coupled with the same resonator, even if the two qubits are dynamically decoupled from the resonator, there is an effective coupling between the two qubits if their modulation phases are different. In Fig. S4, we show the effective coupling between two qubits with modulated transition frequencies $\omega_j(t) = \omega_r + \Delta\cos(\nu t - \phi_j)$, taking

Q_aQ_b as s_1s_2. The second order effective interaction Hamiltonian is $H = i\hbar g_{\mathrm{eff}}\left(\sigma_1^+\sigma_2^- - \sigma_2^+\sigma_1^-\right)$ with $g_{\mathrm{eff}} = \sum_{n=1}^{\infty} 2g^2 J_n^2(f)\sin(n\Delta\phi)/n\nu$ where $\Delta\phi = \phi_2 - \phi_1$. We initialize s_1 in $|\uparrow\rangle$ and s_2 in $|\downarrow\rangle$ and tune Δ_ϕ. The population swapping between the two qubits are demonstrated by measuring the joint probability of $P_{\uparrow\downarrow}$ as a function of the delay time. The effective coupling strength $|g_{\mathrm{eff}}|$ is shown in Fig. S4 (C).

NUMERICAL SIMULATION AND ERROR BUDGET

Numerical simulations using the original time-dependent Hamiltonian with the second excited included state for each qubit is done based on QuTiP [1], where we use the experimentally measured device parameters shown in Tab. S1. Due to possible inaccuracy in measuring the qubit-resonantor coupling strengths and the resonant frequency of the resonator, we slightly increase all measured values of the coupling strengths by 3% and add a small offset of -3.5 MHz to the transition frequency ω_j of each qubit for a better agreement between the numerical simulation and the experimental data, as shown in Fig. S5. Although the overall initial phase ϕ_0 has no effect on the effective Hamiltonian, it has a substantial effect on the fast oscillation of the probabilities [2], which will be investigated elsewhere. The value of ϕ_0 is unknown due to the signal delay in our measurement system, but we adopt $\phi_0 = \pi/3$ to better account for the experimental data. We note that the small mismatch between the numerical simulation and the experimental data as seen in Fig. S5 could be further reduced by allowing the above mentioned parameters to slightly fluctuate from qubit to qubit.

We can provide an error budget based on the numerical simulation. In our experiment, the sources of error include nonideality of the two modulation parameters (the amplitude Δ and the frequency ν), decoherence, and nonideality of the experimental pulses. Taking the fidelity 0.588±0.014 of the 5-qubit GHZ state as an example, about 42% of the total error are due to nonideality of the modulation parameters with the experimentally chosen $\Delta/2\pi = 235$ MHz and $\nu/2\pi = 98.8$ MHz, which are limited by the dynamical range of our hardware tunability that can be improved in the near future. With more numerical simulations we verify that this nonideality error can be significantly reduced by increasing Δ and ν. The limited energy relaxation time T_1 and dephasing time T_2^* contribute to about 53% of the total error based on the master-equation numerical simulation. Therefore, nonideality of the experimental pulses only gives rise to about 5% of the total error.

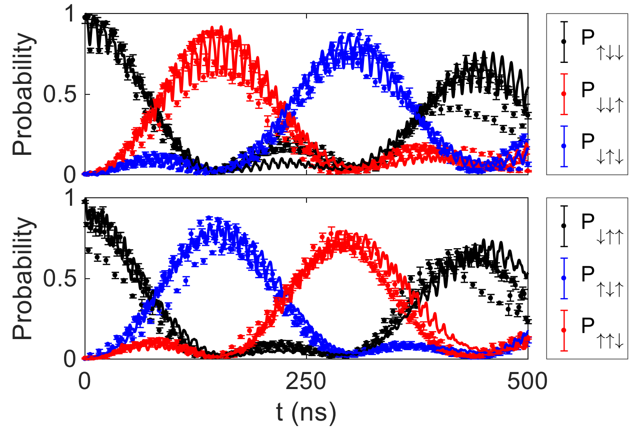

Figure S5. **Numerical simulation of the three-spin chiral dynamics.** Plotted are the experimental data (dots with error bars), which are also shown in Fig. 1 in the main text of the main text, and the numerical simulation (lines).

COHERENT CONTROL OF THE CHIRAL SPIN DYNAMICS

The Hamiltonian that contains a spin-1 operator $\mathbf{S}_1 = \boldsymbol{\sigma}_2 + \boldsymbol{\sigma}_3$ exhibit richer dynamics than the three-spin ASI Hamiltonian H. For a four-spin cluster $s_1s_2s_3s_4$ as shown in Fig. 2 (A) in the main text, in the single spin-up subspace, the chiral evolution follows $|\uparrow\downarrow\downarrow\downarrow\rangle \to \frac{1}{\sqrt{2}}|\downarrow\rangle(|\uparrow\downarrow\rangle + |\downarrow\uparrow\rangle)|\downarrow\rangle \to |\downarrow\downarrow\downarrow\uparrow\rangle \to |\uparrow\downarrow\downarrow\downarrow\rangle$, where the second state involves with a superposition of spins s_2 and s_3. By applying a π phase gate that changes the symmetric superposition to an antisymmetric superposition state $\frac{1}{\sqrt{2}}|\downarrow\rangle(|\uparrow\downarrow\rangle - |\downarrow\uparrow\rangle)|\downarrow\rangle$, the chiral evolutions in the two triangles cancel each other and the whole state becomes stationary, as shown in Fig. S6. After another phase gate that turns the antisymmetric state back to the symmetric state, the chiral evolution is restored.

We can also inject one more excitation to the cluster, and observe chiral dynamics in the double spin-up subspace, which leads to four-spin entanglement. In Fig. S7 (A) and (B), we pictorially draw the interactions between the states in the single spin-up and double spin-up subspaces of the four-spin ASI Hamiltonian H_1. The chiral evolution in the single spin-up subspace is shown in Fig. 2 (A)-(C) in the main text. By comparing Fig. S7 (B) with Fig. S7 (A) we can conclude that the chiral evolution in the double spin-up subspace follows $\frac{1}{\sqrt{2}}|\uparrow\rangle(|\uparrow\downarrow\rangle + |\downarrow\uparrow\rangle)|\downarrow\rangle \to \frac{1}{\sqrt{2}}(|\downarrow\uparrow\uparrow\downarrow\rangle + |\uparrow\downarrow\downarrow\uparrow\rangle) \to \frac{1}{\sqrt{2}}|\downarrow\rangle(|\uparrow\downarrow\rangle + |\downarrow\uparrow\rangle)|\uparrow\rangle$ and back to the initial state. The second state is a GHZ state up to single spin flips, for which the detailed generation protocol is described in Fig. S7 (C). The experimental density matrices and fidelity values of the four-spin states, including the GHZ state, are shown in Fig. S7 (D).

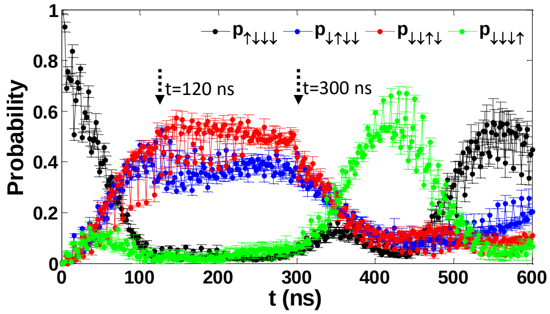

Figure S6. **Freezing and recovering the chiral spin dynamics.** The spins are initialized in $|\uparrow\downarrow\downarrow\downarrow\rangle$ and evolve with ASI in a configuration shown in Fig. 2 of the main text. When the spin cluster evolves to $\frac{1}{\sqrt{2}}|\downarrow\rangle(|\uparrow\downarrow\rangle+|\downarrow\uparrow\rangle)|\downarrow\rangle$ at $t=120$ ns, a π phase gate is applied to spin s_3 and transformed the state to $\frac{1}{\sqrt{2}}|\downarrow\rangle(|\uparrow\downarrow\rangle-|\downarrow\uparrow\rangle)|\downarrow\rangle$. The chiral evolution is frozen for 180 ns. We apply another π phase gate to spin s_3 at $t=300$ ns, which recovers the chiral spin evolution. The qubit sites $s_1s_2s_3s_4$ are orderly assigned with $Q_cQ_aQ_dQ_b$ in the Fig. 1 in the main text. The experiment is performed in the second superconducting circuit.

THE GENERAL HAMILTONIAN FOR SEQUENTIAL SPIN TRANSFER

In Fig. 1 (C) and (D) and Fig. 3 (D) in the main text, the differences between the modulation phases are chosen to be $2\pi/3$ and $2\pi/5$ for a sequential spin transfer in 3-spin and 5-spin systems. However, this cannot be extended to arbitrary number of spins. In general, a sequential spin transfer for an N-spin system requires a Hamiltonian

$$H = H_{mn}\sigma_m^+\sigma_n^-, \tag{S8}$$

with

$$H_{mn} = \frac{2\pi g}{N^2}\sum_{k=1}^{N} k e^{i(n-m)\frac{2\pi k}{N}}, \tag{S9}$$

where g is a coupling constant. That is to say, in general we need both symmetric and anti-symmetric spin exchange interactions.

In Fig. S8, we show the 10-spin sequential evolution. The experimental implementation requires more complicated control sequence than the sinusoidal modulation of the transition frequencies of the qubits, which is going to be investigated in the future.

[1] J. Johansson, P. Nation, and F. Nori, Comput. Phys. Commun. 183, 1760–1772 (2012).

[2] C. K. Law, S. Y. Zhu, and M. S. Zubairy, Phys. Rev. A 52, 4095-4098 (1995).

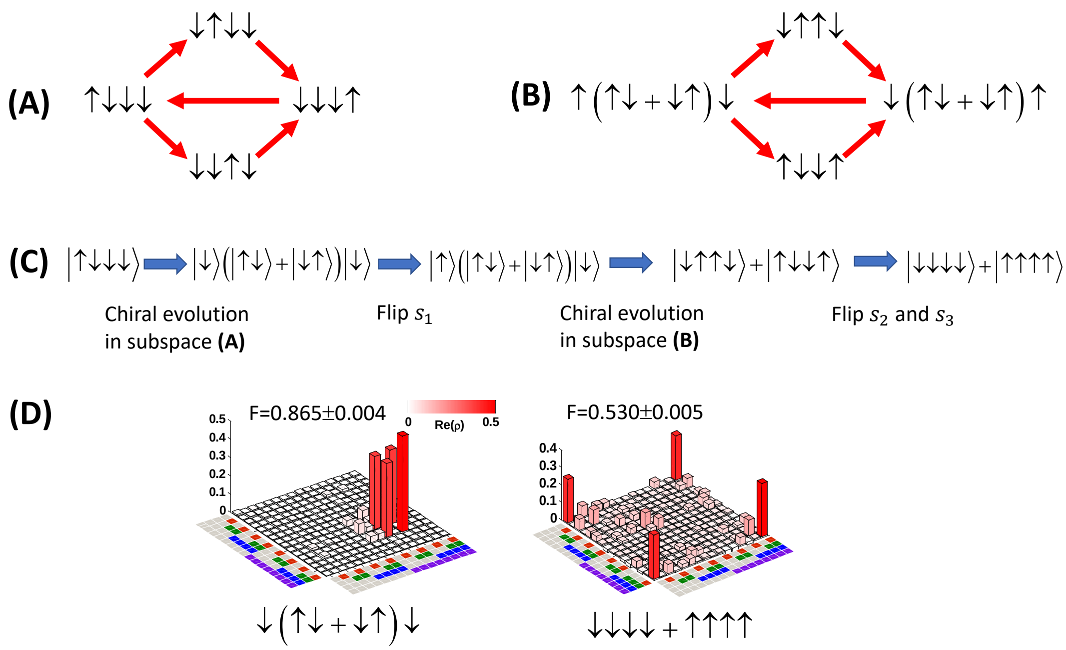

Figure S7. **Four-spin entanglement.** (A) The pictorial four-spin ASI Hamiltonian H_1 in the subspace of single spin-up states. Any two sites connected by a red arrow represents a hopping term and its hermitian conjugate in the Hamiltonian, where the arrow indicates the hopping direction for a phase factor of $e^{i\pi/2}$. (B) The pictorial four-spin ASI Hamiltonian H_1 in the subspace with double spin-up states. The notations are similar as in (A). (C) Chiral evolution which records the actual states of the four-spin system in chronicle order as indicated by blue arrows. The evolution jumps from the subspace in (A) to that in (B) due to an injection of excitation after the operation of "flip s_1". (D) The density matrix and fidelity of the final state in the single spin-up subspace $\frac{1}{\sqrt{2}}\left|\downarrow\right\rangle\left(\left|\uparrow\downarrow\right\rangle+\left|\downarrow\uparrow\right\rangle\right)\left|\downarrow\right\rangle$ and those of the final GHZ state $\frac{1}{\sqrt{2}}\left(\left|\uparrow\uparrow\uparrow\uparrow\right\rangle+\left|\downarrow\downarrow\downarrow\downarrow\right\rangle\right)$. We have neglected the kets and the normalization factors of the states in the figures for simplicity. The qubit sites are assigned the same as in Fig. S6. The experiment is performed in the second superconducting circuit.

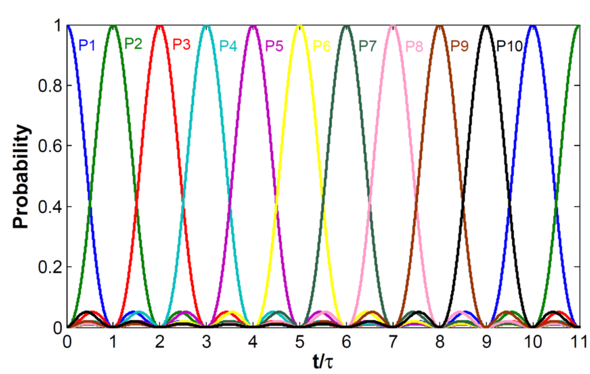

Figure S8. **Sequential dynamics of a 10-spin system.** The 10 spins have all-to-all interactions according to Eqs. (S8) and (S9) with $N = 10$. The time unit $\tau = 10/g$. Pj is the population of the state with the jth spin up and all other spins down.